Experimental Characterization of Impact Attenuation for Small Payloads

Jesus Pacheco* , Holt Merkle† , Jacob Wachlin‡ , Benjamin León§ , Michael Ward¶ , and Mark Costello‖
Earthly Dynamics, LLC, Atlanta, GA, 30309

John Gildea**
US Army Combat Capabilities Development Command Soldier Center, Natick, MA, 01760

Impact attenuation is a critical component of cargo airdrop systems, ensuring payload survivability while allowing practical impact speeds. Cardboard honeycomb is the standard material used for this purpose, but this material is far too stiff to function well on small (5 – 50) lb payloads. This work describes an effort to investigate alternative impact attenuation options for small, lightweight payloads. A purpose-built impact test rig was constructed to facilitate rapid testing and enable repeatable impacts at various combinations of horizontal and vertical impact speeds. A computer vision system was developed to track the payloads as they impact to measure actual impact speeds, and custom sensors were used to measure impact accelerations. A variety of different impact attenuation materials were tested using the test rig and instrumentation systems and the results of these experiments are reported.

I. Nomenclature

v_z	=	payload descent rate
v_x	=	payload horizontal speed
h_s	=	height of payload system
h_0	=	payload detachment height
h_1	=	payload hoist height
e	=	zipline efficiency
a_p	=	payload acceleration
a_s	=	sensor-based acceleration
r_s	=	position of sensor relative to payload CG
ω	=	payload rotation rate
α	=	payload angular acceleration

II. Introduction

Historically, cargo airdrop in the Army has been conducted to bring large quantities of supplies to a central area. For these large bundle airdrop operations ranging from several hundred to tens of thousands of pounds, the standard attenuation material is cardboard honeycomb [1]. Cardboard honeycomb is an inexpensive, biodegradable, lightweight, and effective means of impact attenuation. The purpose of impact attenuation is to dissipate impact energy and provide structural protection to airdropped cargo systems during the ground-impact phase when landing. Cardboard honeycomb functions as a crumple zone, intended to prolong the duration of an impact. Current cargo airdrop rigging procedure involves strategic layering of cardboard honeycomb sheets, with a nominal crushing strength of 60 psi, between the payload, such as bulk supplies or a vehicle, and a landing platform [2]. The amount of material used and the resulting

*Junior Research Engineer, AIAA Member.
†Junior Research Engineer.
‡Research Engineer, AIAA Member.
§Research Engineer, AIAA Member.
¶Senior Research Engineer, AIAA Senior Member.
‖Chief Executive Officer, AIAA Associate Fellow.
**Project Engineer

weight distribution depends on the payload weight and padding surface area. For example, a 6,750 lb payload on an 8 ft long Type V airdrop platform with two layers of honeycomb, yields an average static loading on the attenuation of 17 psi [3]. In another instance, a 600 lb payload in an A-22 cargo bag with a 48 in.×48 in. skid board and one layer of honeycomb yields an average static loading of 8.5 psi [4].

While effective on larger bundles, the traditional cardboard honeycomb material and rigging methodologies do not scale well to smaller payload sizes in the sub-50 lb range. For instance, a 50 lb payload on an A-7A cargo sling with a 32 in.×48 in. landing platform yields an average static loading of 1.1 psi [5]. At this scale, standard 60 psi honeycomb fails to sufficiently crumple on impact and offers poor attenuation capability. From preliminary impact testing, it is evident the weakest, commercially available, cardboard honeycomb, with a nominal crush strength of 11 psi, is still too stiff to cushion impacts at this scale. An alternative attenuation is therefore necessary for lightweight systems to land softly. Technologies such as airbags with a controlled deflation rate have been proposed [6][7]. However, these methods are substantially more expensive, require additional hardware to actively rent and control the airbag pressure, and may not be practical for small lightweight systems. The proposed attenuation material(s) must be competitive against standard honeycomb; it must not require substantial additional setup or rigging effort. The desire to conduct cargo resupply of small payloads and ensure survivability of the contents opens the aperture to identify, investigate and conduct proof of concept testing on new technologies to improve payload survivability of small resupply payloads. Passive attenuation systems which rely on their intrinsic cushioning properties are the focus of this work.

III. Impact Test Rig Development

A. Replicating Impact Conditions

To facilitate the evaluation of the alternative attenuation materials, a test rig was built to reliably replicate landings. The replicated impacts, defined by a descent rate and horizontal speed, are intended to simulate descents under a ballistic parachute being blown by the wind. The design space for the test rig is defined by the following requirements:

1) Payload weight: 5 lb – 50 lb
2) Maximum payload height: 2.50 ft
3) Maximum descent rate: 30 ft/s (20.5 mph) (18 kts)
4) Maximum horizontal speed: 27 ft/s (18.4 mph) (16 kts)

During the initial design phase, rig designs that fulfilled portions of the requirements were still considered to determine whether a reduction in impact velocity capability could be traded off for reduced complexity, cost, or labor. All potential test rig designs followed the same high-level design and operation methodology, in which one end of zipline wires or rails is secured to a tall, sturdy structure with the other end anchored in the ground. Figure 1 illustrates the high-level geometry of the test rig and its operation.

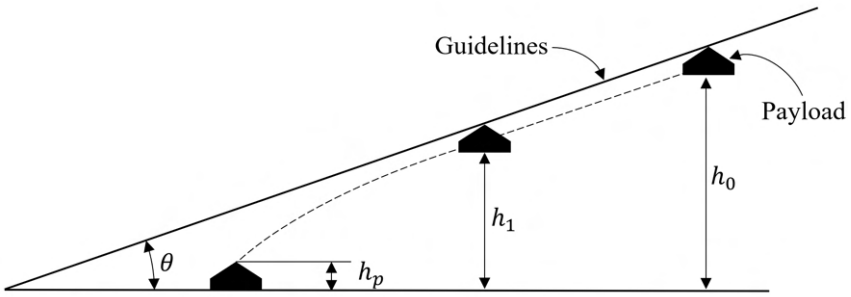

Fig. 1 High-level geometry of the impact test rig

The test rig is operated by ground personnel using a series of pulleys and cables to hoist and release the payload. The parameter h_p accounts for the height of the airdrop system to be impacted, which includes a surrogate payload, attenuation, and onboard support hardware. The support hardware is intended to help attach and detach the system from the test rig zipline. The payload system is first attached to the ziplines and, through a series of cables, is hoisted up along the ziplines to the desired starting elevation h_0. For purely vertical impacts, without a horizontal speed, the payload is then detached from the ziplines at this starting elevation and freefalls until it impacts the ground with a descent rate v_z.

For impacts with a horizontal speed, the hoisted system is first allowed to slide down the ziplines, accelerating up to a final desired horizontal speed v_x and an intermediate descent rate. Once the payload reaches the desired intermediate velocity at a predetermined height h_1, it is then detached from the ziplines and free falls towards the ground, mimicking an impact that might be occurring during an airdrop in windy conditions The payload reaches its final descent rate v_z just before ground contact.

For all candidate test rig designs, the maximum hoisting height is a critical parameter as it cannot be modified once the rig is built and therefore defines the maximum achievable impact velocities. The zipline angle θ and payload system height are of secondary importance. Both parameters further constrain the achievable velocity envelope, namely the horizontal speed, because the payload must be detached from the ziplines before striking the ground, thereby rendering a lower portion of the ziplines unusable. The detachment height does not influence the velocity envelope and is only needed to select a particular impact velocity. The final impact velocity is calculated via Eq. (1) and Eq. (2). An efficiency parameter e is included to account for loss of energy when sliding along the ziplines on account of friction. Figure 2a details how the achievable impact velocity envelope shifts with an increasing maximum hoist height capability.

$$v_x = \sqrt{(2ge)(h_0 - h_1)/\sec^2(\theta)} \tag{1}$$

$$v_z = \sqrt{(2ge)(h_0 - h_s) - v_x^2} \tag{2}$$

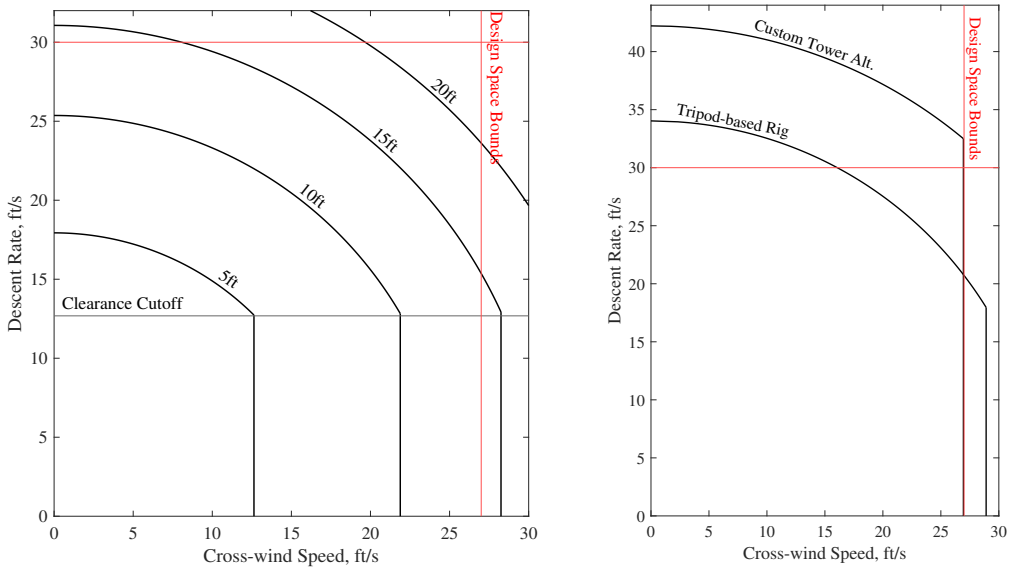

(a) Test rig capability at various max hoisting heights **(b) Capability of different test rig designs**

Fig. 2 Velocity envelope study

B. Test Rig Design

From an Analysis of Alternatives process, two test rig design candidates were identified. The first candidate was a custom-built steel tower with a 48 degree zipline angle and a maximum hoisting height of 28 ft, a sufficient elevation to fully encompass the maximum impact velocities. The second candidate was a smaller, tripod-based tower with a maximum hoisting height of 18 ft and a 24 degree zip line angle. Despite its reduced capability, the smaller tower was selected for its cost-effectiveness and ease of operation.

The structural skeleton of the test rig is constructed from two COTS heavy-duty modular tripods. To improve stability and ensure ample open space for safe operation, the two tripods are rotated 60 degrees relative to each other and distanced 3.5 ft from each other. Each tripod head is bolted to either end of a 3.5 ft long aluminum beam. With this

setup, both tripods have two outer facing legs and one inner leg facing its sibling tripod. The inner legs are removed. The resulting 18 ft tall structure features four legs with an 8.5 ft×8 ft rectangular base. A steel zipline cable is anchored from each of the tripod heads to corresponding ground anchors, which are also distanced 3.5 ft apart from each other. Additional tie-downs are installed to ensure structural stability. A hoisting pulley is mounted to the midsection of the aluminum beam. Figure 3 shows the completed test rig. Figure 2b shows the achievable impact velocity envelope for the built test rig and the alternative custom tower option.

Fig. 3 Controlled impact test rig

C. Support Hardware

The support hardware, both on board the payload and on the ziplines is responsible for attaching and detaching the payload from the ziplines at a designated moment. The support hardware on the ziplines or "carriage" is constructed from 2-by-4 wood studs, using zipline trolleys to travel along the steel ziplines cables with low friction. The support hardware on the payload system features a ratchet assembly designed to pull two plates tightly together; one plate is attached to the payload and the other is attached to the carriage. The ratchet assembly cinches down a rope onto a pin to hold the plates together. When the pin is pulled, the plates cleanly separate and detach payload from the carriage. The cinch point is vertically aligned with the CG of the payload system to minimize induced rotation rates from the release action.

A remotely controlled latch release is used to start an impact trial. For impacts without a horizontal speed, the latch release hangs from the carriage and suspends the payload midair. Once ground personnel triggers the latch release, the payload is detached and begins falling. For impact tests with horizontal speed, the latch release is in line with a hoisting cable and the carriage. A positioning arm is secured underneath the carriage and suspends the payload midair. Once ground personnel triggers the latch release, the carriage begins to slide down the ziplines. At a designated height, a release cable pulls a pin, quickly detaching the payload from the blue arm. Figure 4 and Fig. 5 show the different setups strategies when conducting impact tests with and without a horizontal speed.

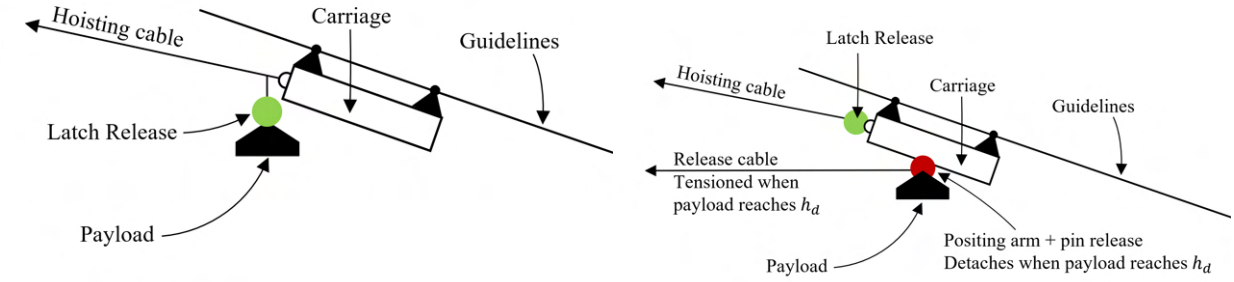

(a) Setup schematic for no horizontal velocity impacts **(b) Setup schematic for impacts with horizontal velocity**

Fig. 4 Test rig support hardware schematics

(a) Setup for impacts without horizontal velocity **(b) Setup for impacts with horizontal velocity**

Fig. 5 Test rig hardware Setup

IV. Instrumentation

A substantial aspect of evaluating different attenuation materials regards their ability to lower the payload accelerations during the initial ground-impact phase when landing. A surrogate payload as shown in Fig. 6 was constructed to measure the deceleration profiles via a series of sensors and tracking markers. The surrogate payload is a layered stack measuring 12 in.×5 in.×3 in. and made of steel, aluminum, and plywood plates. On top of the stack is the cinching assembly for interfacing with the zipline hardware. The surrogate payload is bolted to the center of a 15 in.×15 in.×0.5 in. plywood base. Two high-G 3-axis accelerometers are bolted within the surrogate payload stack, each within 2 in. of the payload CG. Each sensor records accelerations at 1 kHz. Two 3-axis gyroscopes are also bolted to the payload, one on top of the surrogate stack and another on the plywood base. These sensors record angular rates at 200 Hz. Tracking markers, discussed in detail in a subsequent section, are bolted along the periphery of the payload base. Altogether the payload weighs 22.7 lb, not including the attenuation material. Attenuation material is secured underneath the payload base using four 1 in. wide nylon straps that wrap around the attenuation and payload base.

Two commonly used technologies that were proposed for data collection but were ultimately rejected were GPS and IR sensors. GPS positioning could help validate the impact velocity, but the update rate and accuracy are not suitable at this scale. IR sensors onboard the payload could help measure its elevation as it is sliding on the ziplines and validate the impact descent rate. However, difficulties concerning overwhelming IR from the sun and ground reflections in an outside setting prevented its use.

A. Photogrammetry

One evaluation criterion concerns the crushing and rebound dynamics of the attenuation that occur during and after impact. These short-lived dynamics are difficult to describe using only IMU sensors onboard the payload. A supplemental data acquisition method was developed using high-speed cameras. In addition to the qualitative feedback high-speed video can provide, quantitative measurements regarding the relative motion of the payload are possible

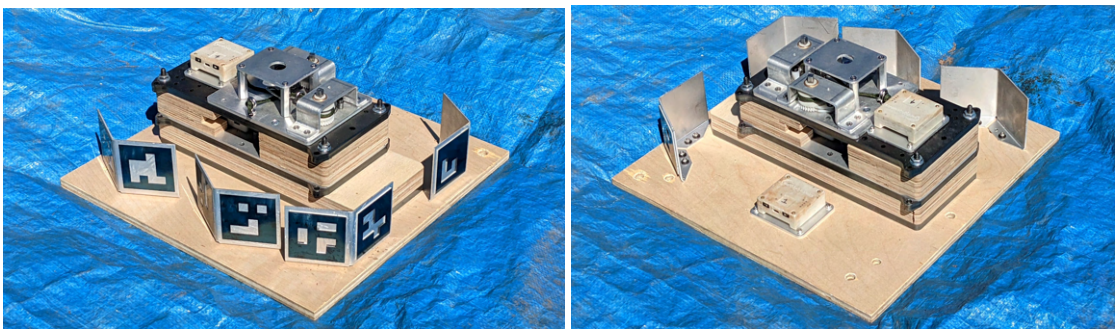

(a) Front view showing ArUco markers **(b) Back view showing gyroscope sensors**

Fig. 6 Mock Payload for impact testing

provided adequate setup. The methods discussed in this paper were developed through continuous testing and are tailored for a portable camera system where extensive setup procedures at the test field are impractical. The vision system hardware includes two 1.4 Chronos cameras and two Computar 12.5-75mm f/1.2 zoom lenses.

1. Scene Reconstruction

To quantify the motion of the payload, its pose must be reconstructed from high-speed video. The standard method for 3D feature-based reconstruction, known as Bundle Adjustment [8], is an optimization approach that attempts to reconstruct a scene based on observed point-of-interest (POI), a 3D point model, and viewing parameters for the camera. The method involves minimizing the reprojection errors between observed and predicted image locations by iteratively refining the estimated pose of the point model relative to the camera. The viewing parameters describe the relationship between 3D points relative to the camera and their corresponding 2D image projections and are broken down into two sets: (1) the extrinsic parameters which describe the location and orientation of the camera, and (2) the intrinsic parameters which describe the camera lens. Each set of viewing parameters has its own setup process. The intrinsic parameters require a calibration process involving a large calibration board with a printed pattern. The extrinsic parameters are established through a controlled setup process or by referencing locations with known coordinates. A new set of parameters is required if the camera moves or its lens settings change at any moment during a test session.

2. Establishing Points of Interest

The first task in this process is establishing a 3D point model of an object based on trackable POI in an image. A method for detecting POI in an image and facilitating the matching process back to the point model involves the OpenCV library and ArUco markers [9] placed at strategic locations on the object to be tracked. These markers are physical tags displaying a dark square with a white border and an inner binary codification for identification, see Fig 6a. The open-source OpenCV library is a computer vision package that provides a convenient pipeline for processing video and detecting and identifying visible markers. Figure 7a shows the CAD model of the payload used to generate the corresponding point model, shown in Fig. 7b. The four corners of the dark square in the ArUco maker become the POI. The point model describes the position of the POI relative the payload frame. The inner codification also allows OpenCV to report said corners in a predictable order, starting from the top left, moving clockwise relative to the marker. With this controlled reporting order, the relative position and orientation of an individual marker can be estimated from the pixel positions of its four corners. Hence the point model also describes the pose of the markers relative the payload. An alternative method for extracting motion of the payload involves calculating the pose of the payload using the individual marker pose estimations. Bundle Adjustment does not use individual marker pose estimations. it only requires a 3D point to 2D point correspondence.

The marker design is critical to its performance and is influenced by the following lessons learned throughout multiple design iterations and continuous field testing:

- Successful detection depends entirely on sharp image contrast to separate all the defining features on the marker. Reflections and partial shadows will significantly hinder the likelihood of success. Minor shadows casted within the makers will degrade the detection solution as the apparent shape of the marker becomes skewed. Other noteworthy limitations include motion blur, out-of-focus fuzziness, partial obstructions, dirt, and scratches.

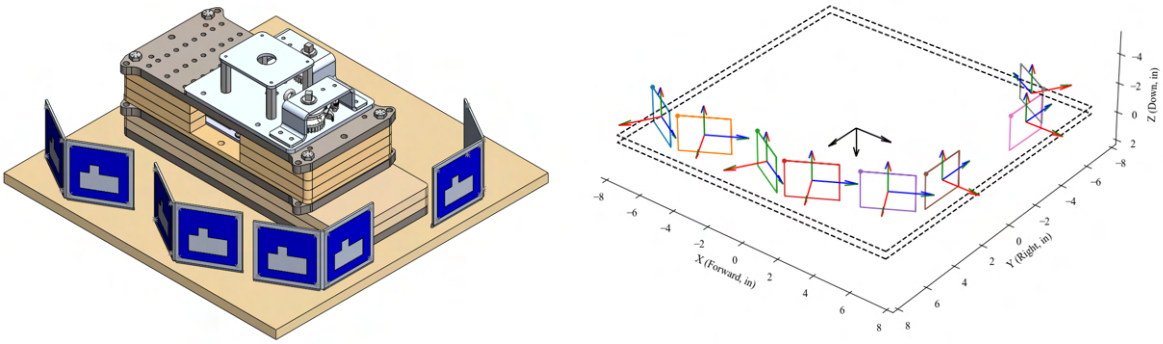

(a) A CAD model of the surrogate payload **(b) A 3D point model of the ArUco Markers**

Fig. 7 Computer models used to establish points of interest

- The entire marker, including a complete white border, must be visible, legible, and unobstructed.
- Markers must be rigid and able to withstand high shock loads without bending or vibrating.

With survivability and simplicity as priorities, the markers are constructed from 0.10 in. thick aluminum sheet-metal brackets and gauge 28 blue temper spring steel cutouts measuring 60 mm×60 mm. The color difference between the aluminum and steel provides sufficient contrast, particularly when viewing through a single RGB channel. The steel cutouts are affixed to the brackets via a white, 0.045 in. thick, Very-High-Bond adhesive tape using a spacing guide to ensure accurate placement. The brackets are bolted onto the wooden payload platform. Etching the aluminum brackets with the marker pattern is a potential alternative as the surface of the marker would be flat and not cast shadows.

The markers can withstand repeated impact testing but are susceptible to high-frequency ringing, particularly during violent landings when the attenuation does not crush well. These oscillations are visible in the high-speed video and often involve the entire aluminum bracket swaying back and forth. These oscillations are present in the data when extracting the image positions of each corner of each marker. The following section discusses the sensitivity of the final solution to this ringing.

The OpenCV pipeline performs most of the detection operations. The critical user task is carrying out a series of image threshold operations to produce a grayscale image with the markers isolated from the background. Figure 8 illustrates the image processing progression: A high-speed image frame is converted to a grayscale image from which the marker corners are detected. The final step involves the Bundle Adjustment algorithm.

3. Capturing Impact Dynamics

The Bundle Adjustment algorithm produces a complete 6 degrees of freedom Z(DOF) pose estimation of the payload provided accurate viewing parameters. Generating these viewing parameters entails considerable setup work complicated by the demands of field testing using the test rig and the limitations of the cameras. The cameras can only capture a segment of the payload trajectory with sufficient detail to reliably extract maker corners. It must be mobile to follow and focus on the impact region throughout a test session. If the camera is repositioned or refocused, a new set of viewing parameters is required. These requirements significantly increase the operational logistics.

However, a simpler approach can produce a usable but a more limited 3 DOF pose estimation of the payload. The standard camera model assumes a perspective projection, where light rays converge to a point. Under an orthographic projection, incoming light rays from a faraway source are functionally parallel. A camera can approximate the alternative projection model if it has a sufficiently large focal length and views objects from a sufficient distance [10]. Additionally, the test rig constraints the movement of the payload in two directions, down and forward, as it slides down the ziplines. These two directions form a plane referred to as the zipline plane. *If (1) the payload remains on this plane after it is released and during the freefall and impact stages, and (2) the camera sensor is parallel to the zipline plane and set to approximate the orthographic projection, then the relative 2D movement of the payload in the image is proportional to the actual movement of the payload.* This reduces the nine original viewing parameters to a single coefficient: a pixel-to-distance scaling factor calculated from the video by referencing the known size of the markers to their size in the image. Provided the camera sensor is parallel to the zipline plane, it is free to move and refocus without calibration.

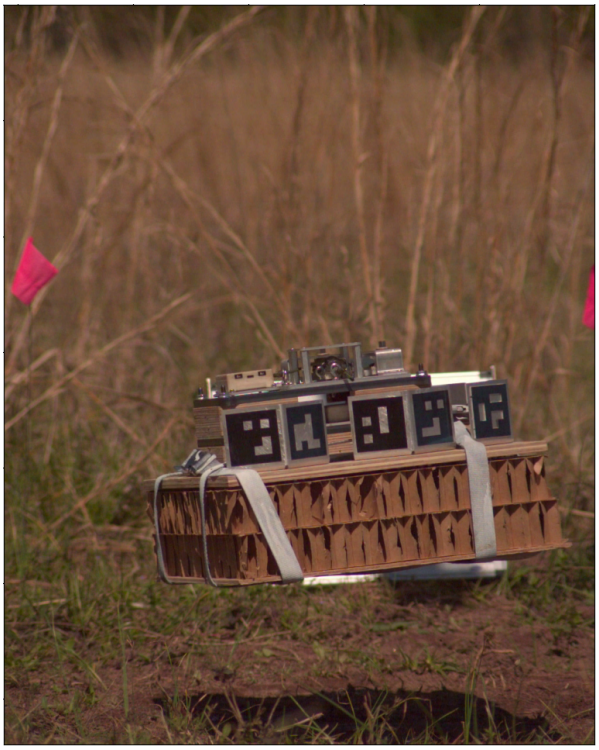

(a) Sample high-speed frame

(b) Isolating the ArUco makers

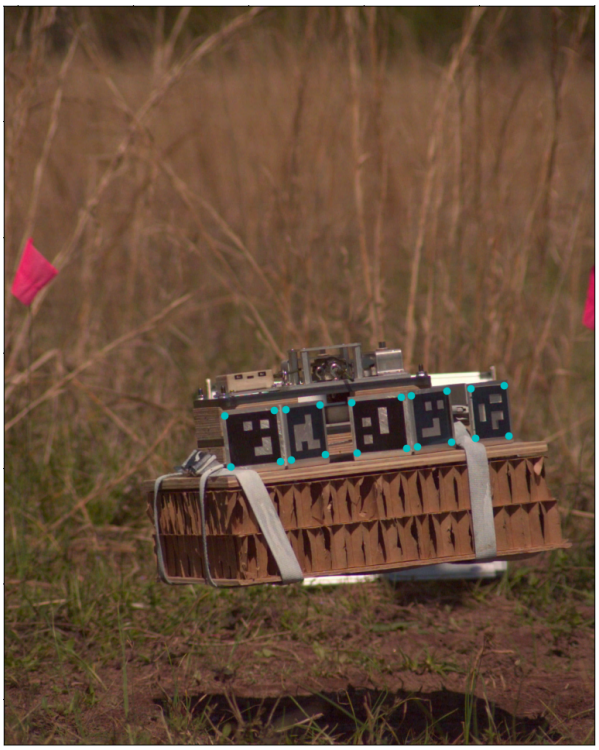

(c) Detecting marker corners

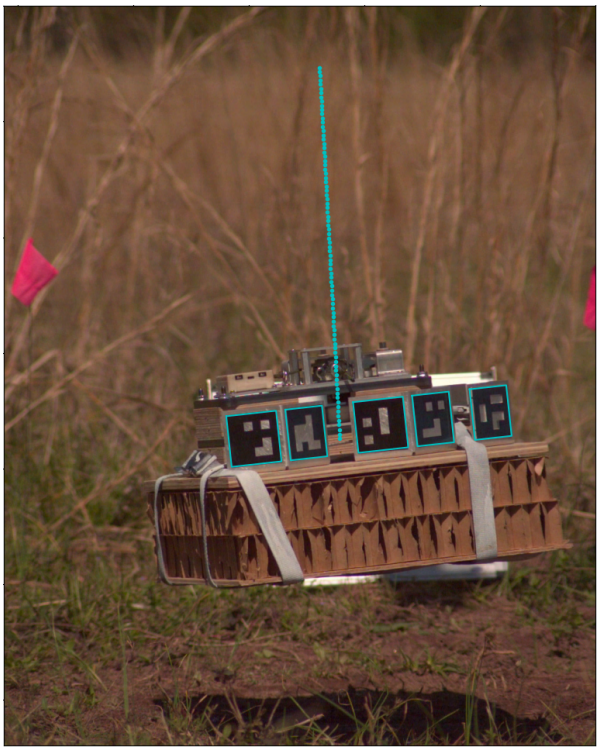

(d) Fitted payload model with payload trajectory shown

Fig. 8 The complete vision system process at each major stage

Table 1 Cameras Settings Summary

Trial	Attenuation Material	Camera 1	Camera 2
1	Cardboard Honeycomb	1024×576@2357fps	1280×1024@1069 fps
2	Soft Poly Foam	1024×576@2357fps	1280×1024@1069 fps
3	Impression Foam	1024×576@2357fps	1280×1024@1069 fps
4	Soft Poly Foam	800×480@3585fps	1280×720@1519 fps
5	Cardboard Honeycomb	800×480@3585fps	1280×720@1519 fps
6	Impression Foam	800×480@3585fps	1280×720@1519 fps
7	Soft Poly Foam	320×240@16682fps	320×240@16682fps
8	Soft Poly Foam	320×240@16682fps	320×240@16682fps
9	Cardboard Honeycomb	320×240@16682fps	320×240@16682fpss
10	Cardboard Honeycomb	320×240@16682fps	320×240@16682fps
11	Impression Foam	320×240@16682fps	320×240@16682fps

4. Extracting Impact Dynamics

The simplified approach generates the position of the CG of the payload in an image and a rotation estimation. Figure 8 shows the final projection of the payload point model along with its trajectory in the video thus far. This 2D image trajectory is scaled using a pixel-to-distance multiplier. A Savitzky–Golay filter is then applied to the raw location solution to generate a velocity and acceleration profile. The Savitzky–Golay filter is a rolling window polynomial regression that smooths a signal and produces its derivatives. To validate the acceleration profile accuracy describes the original position solution, the acceleration profile is double integrated using the cumulative trapezoidal method. A brute force optimizer estimates the initial velocity when the markers are first seen in the image. Figure 9a reports the average per frame residual between the reconstructed position solution and unfiltered position solution as a function of the normalized image resolution.

The normalized image resolution describes the percent of the camera sensor area used to record the high-speed video. The Chronos cameras can record video at various presets. The highest resolution video of 1280×1024 pixels is recorded at 1069 fps. Due to the finite camera data rate, higher frame rates can only be recorded at smaller resolutions. Table 1 details the various combinations used when recording the impact trails to evaluate the performance of different camera configurations. The exposure time and field of view were constant to isolate the comparisons from motion blur and maintain the image size of the markers proportional to the image resolution.

There is a coupled trade-off regarding the robustness and accuracy of the vision system and the frame rate and resolution presets. The robustness of the filtering process improves with higher frame rates as more data is available. But, better image resolution improves the detection accuracy, reducing noise in the unfiltered position solution. As shown by Fig 9a, camera presets which utilize less than 20% of the camera sensor area significantly degrade the filtering results despite the substantial increase in frame rate. These results suggest image resolution should have higher importance than frame rate when choosing a preset. Other on-site considerations include image aspect ratio and the field of view.

The camera setup for these tests used two independent cameras side-by-side to record the same impacts. Figure 9b shows the payload position solutions through the freefall and impact stages from two cameras from two independent impact tests with the same impact conditions. Each camera used different presets. Profiles of the same color correspond to the same impact. The position solutions visually follow a similar profile, despite the varying setups. It is worth noting that each of the two impacts had some markers ringing immediately after the impact. However, the ringing phenomenon does not manifest in the final solution. These results further demonstrate the robustness of the vision system setup and processes.

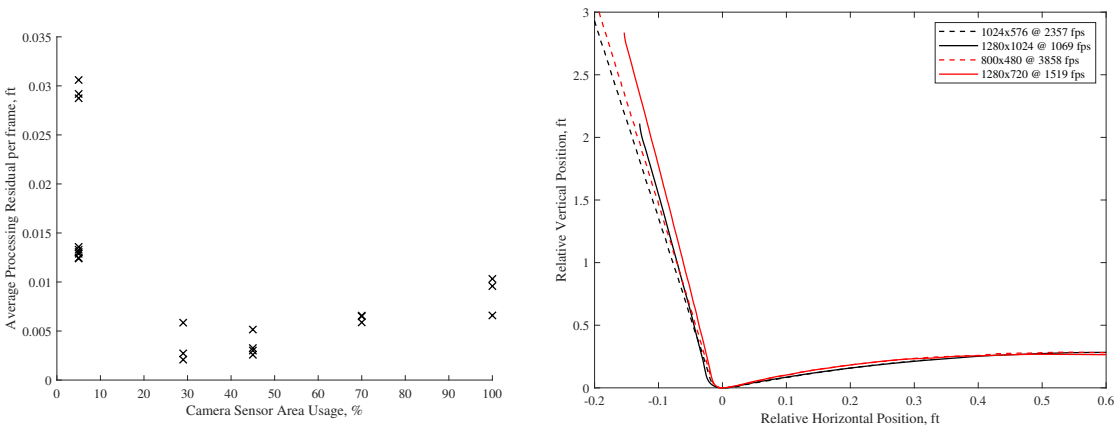

(a) Solution sensitivity for different camera presets **(b) Camera-based payload position solution**

Fig. 9 Position solution sensitivity

V. Attenuation Characterization

The objective of the attenuation is to safely crush and dissipate the kinetic energy of the payload over a prolonged duration. However, the mechanics of deformable bodies crushing under fast loading scenarios are complex. Selection for potential attenuation materials was done through empirical testing and began with a large candidate pool and preliminary vertical impacts with descent rates between 17-20 ft/s and a 15 lb surrogate payload. Of this pool, soft polyurethane foam and impression foam were the finalists for the listed reasons:

1) Ease of rigging - Both materials can be cut, stacked, and rigged without substantial additional rigging effort compared to cardboard honeycomb. Polyurethane foam is available in 2 in. thick sheets. Impression foam is available in 14 in.×6 in.×2 in. slabs.
2) Reproducibility - Both materials can reproduce similar impact dynamics for a particular impact condition, in part due to their homogenous composition.
3) Crush strength - Both materials demonstrated the most promising attenuation capabilities with descent rates below 20 ft/s. They both produce acceleration profiles, as recorded by the onboard sensors, with relatively low peak accelerations.

Honeycomb with the lowest nominal crush strength available of 11 psi was used as a baseline.

A. 11 psi Cardboard Honeycomb

The principal difference between cardboard honeycomb with a nominal crush strength of 11 psi and its 60 psi sibling is the inner honeycomb cell density. Compared to the standard 60 psi honeycomb used in airdrop operations, 11 psi honeycomb is 65% less dense by weight. A less dense inner core corresponds to a lower crush strength. Figure 10a shows two layers of 2 in. thick, 11 psi honeycomb rigged underneath the payload.

B. Soft Polyurethane Foam

The selected polyurethane foam, as shown in Fig. 10b, is part of a large category of rubber-based open-cell foams, commonly found in furniture. Their internal structure is composed of tiny, interconnecting cells that allow for some airflow when compressed. Of the various open-cell foams available, the selected foam, referred to as Soft Poly Foam, has a relatively low crush strength. It has an ILD rating (a stiffness metric in the mattress industry) of 12 lbs [11] which corresponds to a nominal crush strength of 7.75 psi. However, open-cell foams can show a viscoelastic response in fast-loading scenarios in which the crush strength changes with the compression rate and depth [12]. After a deformation-causing load is removed, the foam will quickly return to its original dimensions. It can be cut into any shape using a hot-wire or serrated knife and can withstand repeated impact testing without showing signs of tearing or plastic deformation.

(a) 11 psi cardboard honeycomb **(b) Soft poly foam**

Fig. 10 Payload with attenuation

C. Impression Foam

Impression foam, as shown in Fig. 12, is a closed-cell phenolic foam characterized by its delicate and moldable nature. Unlike its open-cell sibling, closed-cell foams do not have interconnecting cells, preventing airflow. Impression foam is formulated to permanently deform and finely capture the indentation of an applied load. Therefore, it must be handled carefully during the rigging process to minimize premature deformations. This particular foam has a nominal crush strength of 2.8 psi. However, in fast-loading scenarios, this foam will tear substantially.

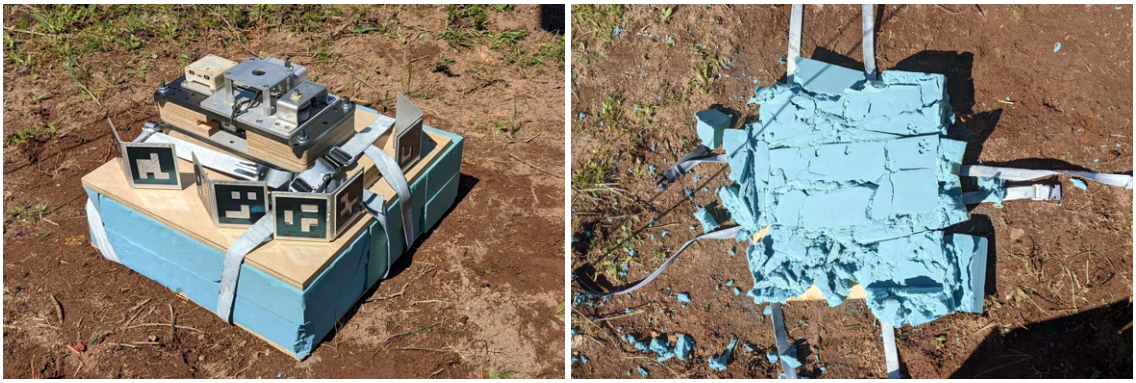

(a) Before an impact **(b) After an impact, payload not shown**

Fig. 11 Payload with impression foam attenuation

D. Rejected Candidates

Of the various materials tested, rejected candidates that showed some promise include molded pulp and memory foam. Molded pulp fiber, commonly found in biodegradable food trays, demonstrated promising preliminary results, yielding relatively low peak accelerations, provided it fully compressed. However, due to its variable geometry, it will crush unpredictably. Custom geometry is required for molded pulp fiber to become a competitive candidate. Memory foam is another polyurethane open-cell foam commonly found in mattresses. It is also homogenous and can elastically deform with the added benefit of slowly returning to its original shape, thereby reducing the overall elasticity of an impact. However, its relatively high crush strength and substantial viscoelastic response yield high acceleration peaks for the payload weights and impact speeds considered. To become a competitive candidate, its crush strength must be reduced, either by reducing the cell density of the foam or with cutouts.

E. Attenuation Sizing

The ideal impact scenario is a constant deceleration of the payload throughout the complete crushing of the attenuation. This requires the attenuation to crush with a uniform loading regardless of deformation and crush rate.

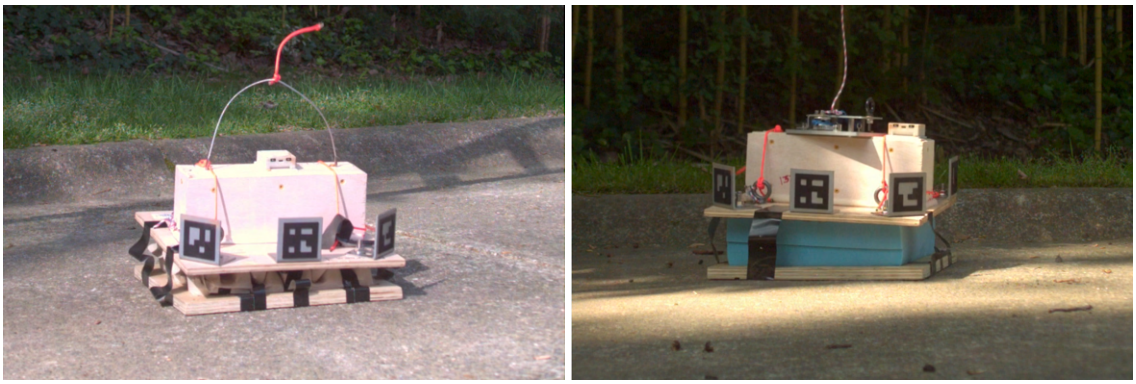

(a) Molded pulp stacked 4 in. thick **(b) Memory Foam stacked 4 in. thick**

Fig. 12 High-speed frames showing a 20 ft/s impact with previous iterations of the surrogate payload, dimensions are the same

However, based on empirical observations, the manner in which the attenuation crushes and/or breaks down is highly dependent on the impact orientation, load distribution, and impact velocity. In the case of open-cell foams, the material volume and exposed surface area also contribute to the crushing dynamics. Additionally, the nominal crush strength rating is only valid under controlled static loading conditions which, in many cases, is intended to describe the stiffness of a material relative to other variations within the same family. The actual crush strength under fast loading scenarios is a complex problem. Calculating the recommended attenuation dimensions for each candidate material for the tested impact conditions is beyond the scope of this work.

When military cargo airdrop operations require cushioning, rigging manuals will detail how much cardboard honeycomb to use and the recommended stacking configurations. In most cases, the recommendations focus on providing structural support for hanging features such as the underbody of a vehicle [3]. For bulk supplies payloads with a smaller footprint such as 48 in.×48 in., up to two layers of cardboard honeycomb, cut to match the footprint area, are recommended [5]. At the small scale, thicker attenuation increases the likelihood of the airdrop system pivoting on impact and smashing the cargo on its side. With this in consideration, the candidate attenuation materials will be cut to match the footprint of the surrogate payload and stacked 4 in. thick.

VI. Attenuation Evaluation

A complete assessment of each attenuation candidate involves investigating their cushioning capabilities at various payload weights and impact conditions. To facilitate direct comparison, the impact conditions were limited to a single descent rate of 20 ft/s with no horizontal speed. The reported results assess each material at a specific impact velocity and payload weight combination and are not a comprehensive evaluation. The results also highlight the various data acquisition methods. A summary of the test setup used for the reported results follows:

- A 15 in.×15 in.×0.125 in. plywood sheet is included underneath the attenuation to distribute the payload weight and encourage a more steady crush.
- Two high speeds cameras recorded each trial. Table 1 details their various frame-rates and resolutions for each trial. Both cameras were side by side, approximately 30 ft from the impact zone.

Table 2 provides a qualitative account of the impact dynamics for each material and details how the rigging procedures. Figures 13 through Fig. 15 show sample high-speed frames showing how the various attenuation materials behave on impact. Note that impression foam debris can prevent a camera-based photogrammetry position solution.

Fig. 13 A cardboard honeycomb impact: (left) before ground contact, (center) at maximum crush depth, (right) at max rebound height

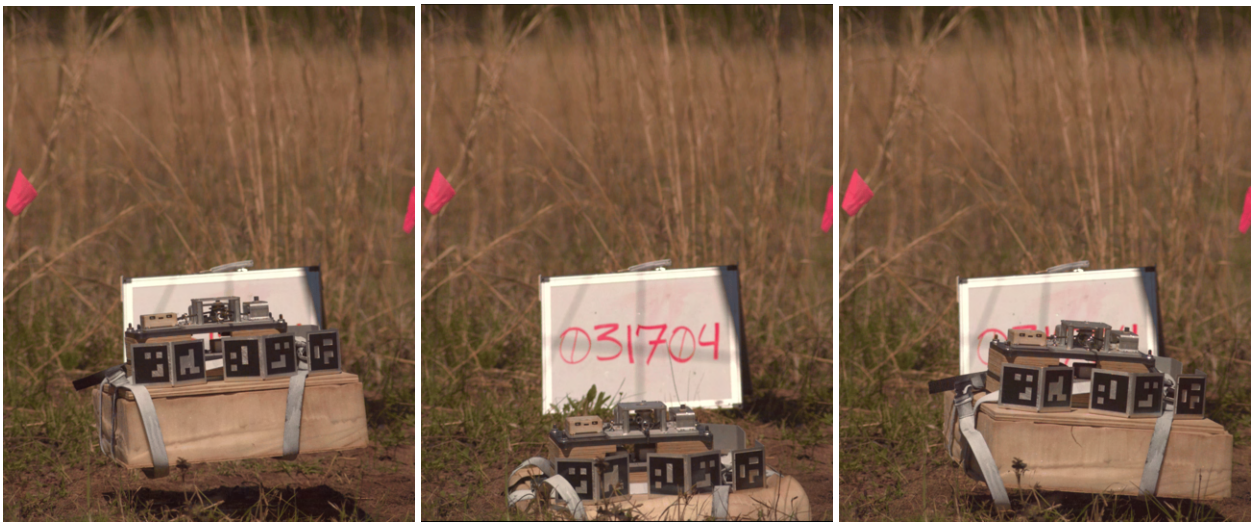

Fig. 14 A soft poly foam impact: (left) before ground contact, (center) at maximum crush depth, (right) at max rebound height

Fig. 15 An impression foam impact: (left) before ground contact, (center) at initial ground contact, (right) at final crush depth

Table 2 Attenuation Behavior Summary

Attenuation Material	**Preparation**	**Rebound after impact**	**Behavior**
11 psi cardboard honeycomb	Two 2 in. thick sheets are trimmed to match the payload platform and stacked vertically	< 6 in.	The impact is abrupt, with no visible signs of crushing or buckling. An individual sheet can survive at least 5 impact tests without showing signs of crushing.
Soft poly foam	A single 4 in. thick sheet is trimmed to match the payload platform	< 12 in.	Frequently compresses upwards of 75% of its initial thickness and will almost always result in a rebound, a single sheet can survive at least 20 impact tests without showing signs of tearing
Impression Foam	Six slabs are organized into 3 rows length-wise and 2 layers high, the remaining area is filled with 2-3 slabs cut width-wise and laid on their sides. This ensures the largest pieces possible are used.	None	During an impact, the material breaks down into large chunks, some of which are violently ejected outwards. There is no correlation between how the individual slabs are arranged and how the chunks are ejected.

A. Payload Acceleration

The principal metric for evaluating an attenuation material is the resultant payload acceleration profile at impact as captured by the two sensors housed within the surrogate payload. A lower acceleration means less force is transferred to the payload which reduces the likelihood of damage. Therefore the best attenuation material, for the tested impact conditions, will result in the lowest acceleration profiles. To facilitate direct comparison, the sensor-based peak accelerations are summarized in Fig. 16. It is clear that for a 23 lb payload with a descent rate of 20 ft/s and 4 in. thick attenuation, impression foam yields the softest landing, with soft poly foam yielding slightly harder landings. The 11 psi cardboard honeycomb produced significantly more violent landings, with peak accelerations exceeding 150 G. Given the complex crushing dynamics of the soft poly foam and the impression foam, this success hierarchy is only applicable for impacts under similar conditions.

Figures 17 through Fig. 19 compare the camera-based accelerations to the sensor-based acceleration. A cross-correlation analysis aligned the four signals. As shown by the similar acceleration data, the results demonstrate the high-speed camera system is a viable tool capable of generating acceleration estimations. Since the accelerations are

derived from relative position estimations, it is possible to determine when the attenuation material first contacts the ground and when it reaches its max compression. With known frame endpoints, the acceleration profile can be trimmed to isolate the acceleration transferred to the payload during the initial crushing of the attenuation material. This can provide further insight into the performance of the attenuation materials.

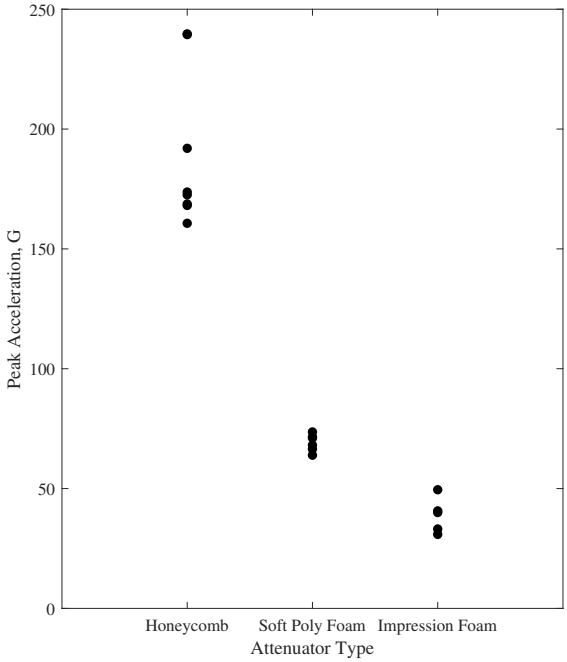

Fig. 16 Sensor-based peak accelerations

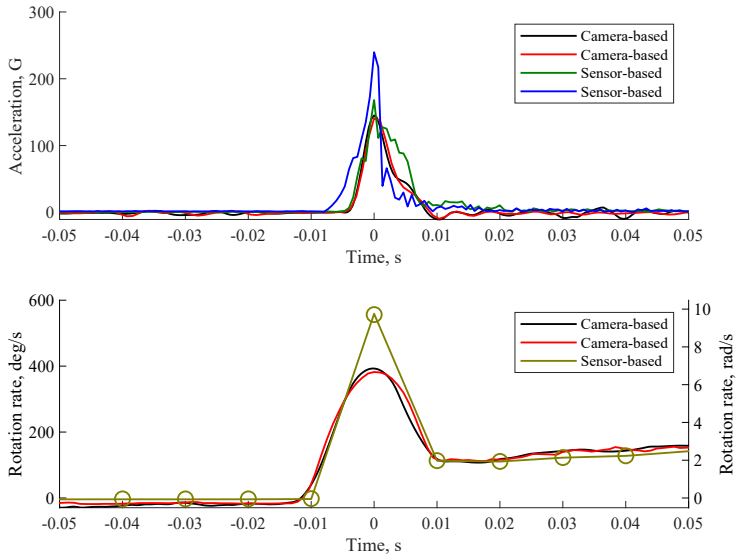

Fig. 17 Impact dynamics using cardboard honeycomb

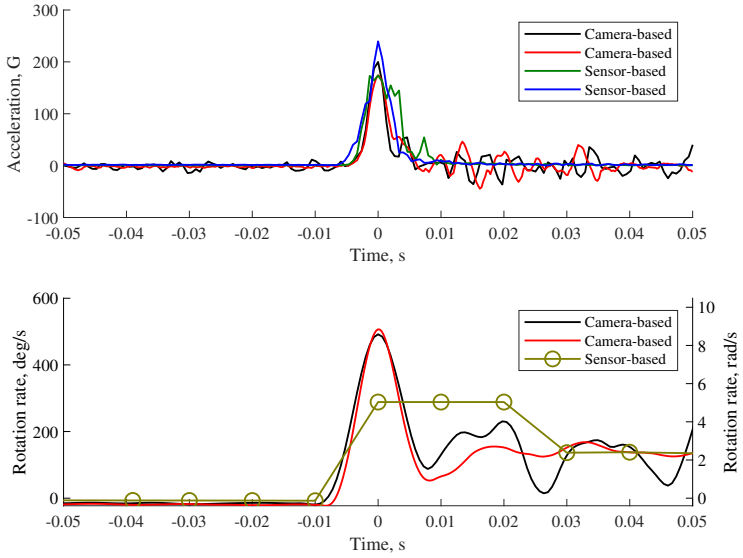

Fig. 18 Impact dynamics using cardboard honeycomb

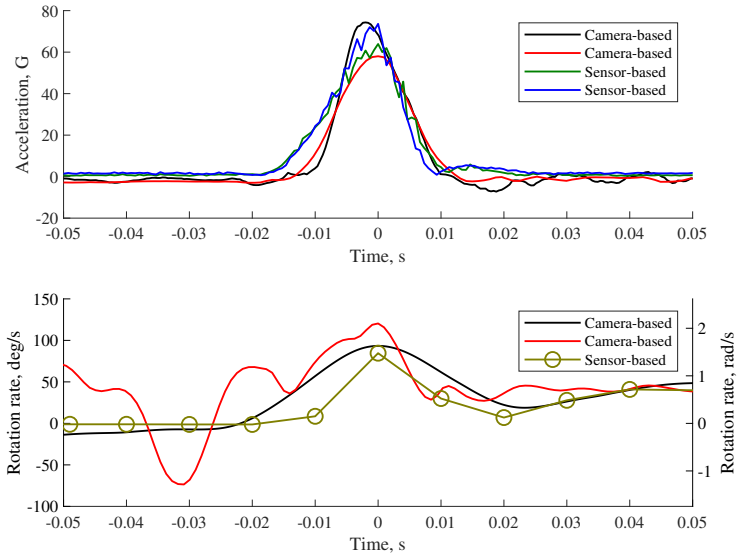

Fig. 19 Impact dynamics using Soft Poly Foam

B. Attenuation Crushing Dynamics

It is possible to describe the crushing dynamics of the attenuation by considering the camera-based velocity profile of the payload as the attenuation is compressing. Figure 20 details how different attenuation materials decelerate the payload. The beginning of the impact is defined when the payload acceleration passes a threshold. This may not correspond to when the attenuation first made ground contact as some crushing may have already occurred before a noticeable payload deceleration. Cardboard honeycomb and soft poly foam produce a smooth velocity profile, signaling relatively steady crush dynamics, if any. The velocity profile for impression foam is a series of various deceleration stages, signaling unsteady crush dynamics. Despite the erratic velocity profile, impression foam yields the longest-lasting impacts corresponding to a lower (i.e., safer) average deceleration, for this set of impact conditions.

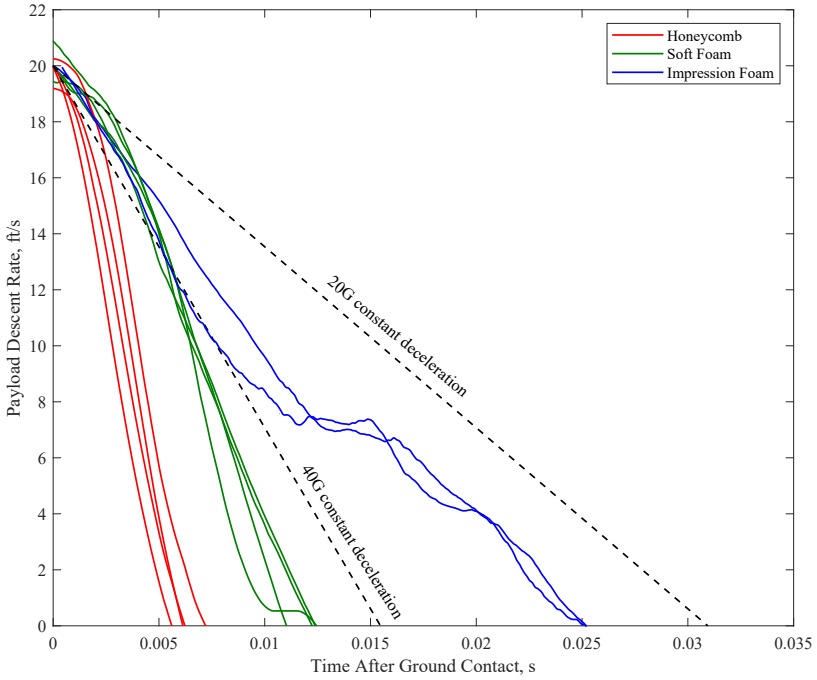

Fig. 20 Camera-based descent rate profiles

C. Descent Rate Validation

To achieve a decent rate of 20 ft/s, the payload must fall from a height of 6.25 ft. At this height, it is possible to manually measure the drop height, ensuring high confidence in the final descent rate. However, at higher drop heights or impacts with a horizontal speed, manual measurements are no longer viable. Additionally, dynamic sagging of the ziplines can introduce discrepancies in the payload detachment heights. In these cases, the camera system could validate the impact velocities by capturing the last portion of the freefall trajectory of the payload. Figure 21 shows the camera-based impact descent rates compared to the theoretical 20 ft/s descent rate. The results demonstrate the high-speed camera system can validate that the hoist and detachment heights produce the desired impact speeds.

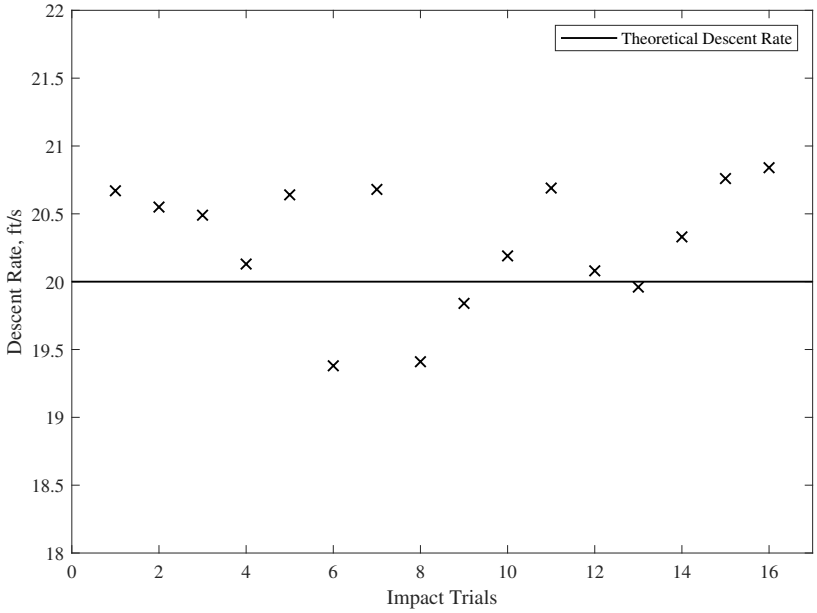

Fig. 21 Camera-based impact decent rate

D. Rotation Rates

The camera system can also generate a rotation estimation of the payload about the axis normal to the zipline planes. The useability of this estimation is limited to how well the axes of the payload are aligned to the zipline plane. Figure 17 compares camera-based rotation rates to sensor-based results when the payload rotates only about one of its axis which is aligned to the zipline normal axis. In this scenario, the solutions closely track each other as the camera-based solution maps well to the sensor-based results. Figures 18 through 19 compare solutions when the payload rotates about an axis that is not always normal to the zipline plane. The figures show the sensor-based rotation rates for the axis that most closely matches the zipline normal axis. In these examples, the camera and sensor solutions do not match well. These examples demonstrate how the camera system can reliably extract a rotation rate under the right conditions.

The rotation rates are also necessary to account for rotation-induced accelerations. When landing, the attenuation will rarely be level with the ground, even in low wind conditions. A single corner or edge of the landing platform will contact the ground first, causing a short but sudden pivoting action until the rest of the platform contacts the ground. The sensors may erroneously record this motion as accelerations caused by the attenuation. Equation 3 is used to compensate for the rotation-induced accelerations. Table 3 lists the maximum sensor-based accelerations that may be induced by the sudden rotations of the payload on impact.

$$a_p = a_s - \alpha \times r_s - \omega \times (\omega \times r_s) \tag{3}$$

Table 3 Rotation-induced compensation for sensor-based acceleration

Sensor	Displacement from payload CG , ft	Max Rotation-induced Acceleration, G
1	0.07	3
2	0.14	12

VII. Conclusion

An impact test rig was built and fielded, demonstrating its capability to reliably replicate the impact conditions of a lightweight payload falling under a ballistic parachute. A high-speed computer vision system capable of extracting the motion of a payload was successfully implemented and produced results comparable to custom sensors measuring

payload impact accelerations. Three candidate impact attenuation materials were tested. Results gathered using both instrumentation systems showed impression foam was the best-suited material to attenuate the surrogate payload at the tested impact conditions. The test and data collection methodology demonstrated in this work can be applied to evaluate the impact dynamics of a wide range of impact velocities, payload weights, and attenuation materials

Acknowledgments

The authors would like to acknowledge the support of the AIRADE Team at the US Army Combat Capabilities Development Command Soldier Center.

References

[1] Ellis, B. C., Ripperger, E. A., and Thompson, J. N., "Design of Cushioning Systems for Air Delivery of Equipment," Tech. rep., August 1961. URL https://apps.dtic.mil/sti/pdfs/AD0270241.pdf.

[2] E.A., R., and R., B. W., "The Crushing Strength of Paper Honeycomb," Tech. rep., March 1973. URL https://apps.dtic.mil/sti/pdfs/AD0763913.pdf.

[3] *Airdrop of Supplies and Equipment Reference Data for Airdrop Platform Loads*, August 2001. URL https://www.marines.mil/Portals/1/MCRP4-11.3LAirdropofSuppliesandEquipmentReferenceDataforAirdropPlatformLoads1.pdf, fM No. 4-20.116.

[4] *Airdrop of Supplies and Equipment:Rigging Loads for Special Operations*, September 2007. URL https://irp.fas.org/doddir/army/fm4-20-142.pdf, no. 4-20.142 (10-542).

[5] *Airdrop of Supplies and Equipment:Rigging Containers*, September 2016. URL https://armypubs.army.mil/epubs/DR_pubs/DR_a/pdf/web/TM%204-48x03.pdf, no. 4-48.03.

[6] Taylor, A. P., Benney, R., and B., B., "Investigation Of The Application Of Airbag Technology To Provide A Softlanding Capability For Military Heavy Airdrop," 2001. https://doi.org/10.2514/6.2001-2045.

[7] H., W., H., H., G., H., H., D., Q., R., and J., L., "Characteristic verification and parameter optimization of airbags cushion system for airborne vehicle," *Chinese Journal of Mechanical Engineering*, Vol. 27, 2014, pp. 50–57. https://doi.org/10.3901/CJME.2014.01.050.

[8] Triggs, B., McLauchlan, P. F., Hartley, R. I., and Fitzgibbon, A. W., "Bundle Adjustment - A Modern Synthesis," *International Workshop on Vision Algorithms*, 2002, pp. 298–372. https://doi.org/10.1007/3-540-44480-7_21.

[9] "Detection of ArUco Markers," , April 2022. URL https://docs.opencv.org/4.x/d5/dae/tutorial_aruco_detection.html.

[10] Burenius, M., Sullivan, J., and Carlsson, S., "Motion capture from dynamic orthographic cameras," 2011, pp. 1634–1641. https://doi.org/10.1109/ICCVW.2011.6130445.

[11] "Product General and Technical Information," , September 2017. URL https://www.thefoamfactory.com/tech/SuperSoftTech.html.

[12] Hilyard, N., "Hysteresis and energy loss in flexible polyurethane foams," *Low density cellular plastics*, 1994, pp. 226–269. https://doi.org/10.1007/978-94-011-1256-7_8.